

Isolated On-Board Battery Charger Integrated with 6-phase Traction Drive

*Original*

Isolated On-Board Battery Charger Integrated with 6-phase Traction Drive / Pescetto, P.; Pellegrino, G.. - (2020), pp. 309-314. (Intervento presentato al convegno 23rd International Conference on Electrical Machines and Systems, ICEMS 2020 tenutosi a Hamamatsu, Japan nel 24-27 Nov. 2020) [10.23919/ICEMS50442.2020.9290958].

*Availability:*

This version is available at: 11583/2881235 since: 2021-04-01T09:50:30Z

*Publisher:*

Institute of Electrical and Electronics Engineers Inc.

*Published*

DOI:10.23919/ICEMS50442.2020.9290958

*Terms of use:*

This article is made available under terms and conditions as specified in the corresponding bibliographic description in the repository

*Publisher copyright*

IEEE postprint/Author's Accepted Manuscript

©2020 IEEE. Personal use of this material is permitted. Permission from IEEE must be obtained for all other uses, in any current or future media, including reprinting/republishing this material for advertising or promotional purposes, creating new collecting works, for resale or lists, or reuse of any copyrighted component of this work in other works.

(Article begins on next page)

# Isolated On-Board Battery Charger Integrated with 6-phase Traction Drive

Paolo Pescetto, Member IEEE and Gianmario Pellegrino, Senior Member IEEE  
Department of Energy Galileo Ferraris, Politecnico di Torino, Torino, Italy  
paolo.pescetto@polito.it

**Abstract**—This paper proposes an innovative topology of on-board battery charger (OBC) for electric vehicles integrated with the traction motor drive. The proposed single phase input OBC, applicable for 6-phase traction drives, is deeply integrated within the vehicle powertrain, to reduce cost and volume of the charger respect to conventional non-integrated solutions. The proposed structure provides galvanic insulation between the grid and the battery, not guaranteed by the other fully integrated chargers in the literature. A dedicated control strategy was developed for absorbing the AC grid current at unitary power factor and low harmonic distortion without torque production during the charging stage. The performance of the proposed OBC are tested by accurate simulation models.

**Index Terms**—On board charger, multiphase synchronous motor, electric vehicle, integrated OBC, PFC, multiphase machine, multi three-phase machine, V2G.

## I. INTRODUCTION

The recent trends in road mobility suggest a considerable increase of the Electric Vehicles (EVs), gaining market share for the near future [1]. This trend, pushed by environmental factors, is increasingly creating new engineering challenges and business opportunities. Therefore, both the academic and industrial research are developing innovative solutions, covering the areas of electric motors, control algorithms, power converters, batteries and charging solutions. Dealing with the machine design, the multi-three phase drives, and particularly 6-phase machines [2], [3], are becoming more and more appealing for improving the reliability of the drive and reducing the phase current rating.

Concerning battery charging, the two main research topics are fast-charging stations and On-board Battery Chargers (OBC). The first ones, commonly including high power rectifier with Power Factor Correction (PFC) and isolated DC/DC converter, can reach a recharge power of the order of 100 kW or more. Complementary to the use of fast charging stations, most of the EVs are equipped with OBC for low (3-6 kW) or medium (10-20 kW) power overnight charging [4].

An OBC can be designed following to two main strategies, namely stand-alone or integrated into the vehicle's powertrain hardware. The integrated solution employs the EV motor as a reactive component and the on-board power electronic converters for regulating the charging current, so it is by definition more compact. Most of the integrated OBCs found in literature [5]–[9] have been developed for 3-phase motors and do not

exploit the additional degree of freedom of having multiple three-phase windings available. Moreover, unless an on-board or off-board [10] isolation stage is considered, none of the reported integrated solutions guarantees galvanic insulation between the ac grid and the battery [10]–[12], with the only exception of the recent [13]. It should be remarked that the isolation is often required by the carmakers, and guaranteed by stand-alone OBCs. Finally, several integrated OBCs found in the literature produce shaft torque during charging operation, thus requiring rotor locking and producing vibrations and acoustic noise.

This paper presents an innovative single-phase isolated OBC integrated into a 6-phase synchronous motor drive designed for EV applications with embedded PFC capability. Differently from many other topologies, the proposed structure is bidirectional, thus permitting Vehicle to Grid (V2G) operation. Dedicated control strategies were developed for regulating the charging power and the grid current quality, and for maintaining zero shaft torque. Comprehensive simulation results prove the feasibility of the proposed solution and its performance.

## II. EV UNDER TEST

Table I highlights the main characteristics of the EV under consideration. The traction motor is an internal PM Synchronous Machine (PMSM) having two symmetric three-phase sets of stator windings [14], [15]. Every quantity referred to each set will be referred to with the subscripts 1 and 2. Each winding set is fed by a conventional 2-level 3-phase inverter, the two inverters named INV.1 and INV.2. Fig. 1 describes the drive topology in traction mode. As the two 3-phase sets are identical, every solution proposed here can be identically applied reversing the sets 1 and 2.

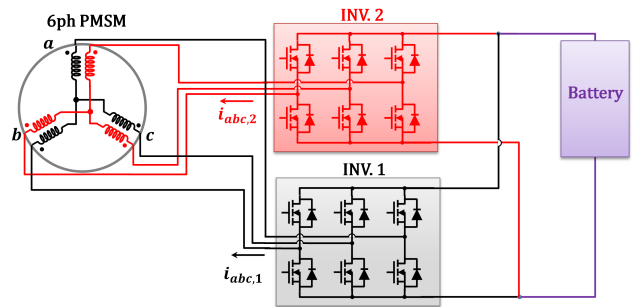


Fig. 1. Six-phase traction e-drive

TABLE I  
RATINGS OF THE TRACTION DRIVE.

motor	rated power	67	kW
	rated torque	80	Nm
	base speed	$\approx 5500$	rpm
	max speed	$\approx 12000$	rpm
	pole pairs	3	
inverter	max phase current	235	Arms
	DC voltage	800	V
	switching frequency	12÷50	kHz

The drivetrain and therefore the electrical machine are designed for a 800V DC bus. Fig. 2(a) shows the flux maps of the tested motor. According to EVs standards, the motor under test is designed for high maximum speed. As a consequence, the phase inductance is in the order of a few mH, depending also on the rotor position.

The IEC 61851-1 standard [16] and the considered EV impose the requirements for the OBC. First of all, the integrated charger should not require additional hardware respect to the e-axis itself, and reaching a charging power up to 6.3 kW supplied by a single phase grid inlet. Galvanic isolation between grid and battery must be provided during charging, guaranteeing a grid current THD < 5% and a Power Factor (PF)>0.95. The OBC control algorithm must be able to operate both in Constant Voltage (CV) or Constant Current (CC) modes, depending on the battery State Of Charge (SOC), without producing torque, relevant vibrations or thermal stress of the motor and the converters. V2G capability is also required. Finally, according to the recent trends, the Transmission System Operator (TSO) may require to the EVs to contribute to regulating the grid reactive power [17]. In this case, the the OBC should be capable of imposing the desired PF<1, still with minimum THD.

### III. MODELING OF THE DUAL 3-PHASE PMSM

In this Section, the adopted model of the dual 3-phase PMSM is described. In the equations, bold symbols stand for vector or matrix quantities, the subscripts 1 and 2 refer to the first and second 3-phase sets, while if the subscript number is missing the quantity refers to the magnetizing component.

Fig. 2(b) defines the spatial coordinates adopted for modeling the dual-three phase machine. The  $abc$  magnetic axes of the two 3-phase sets are coincident. The Clarke transformation permits to compute the  $\alpha\beta$  components starting from 3-phase quantities. The  $d$  axis, i.e. the rotor direction having minimum inductance, defines the rotor position angle  $\theta$ .

The voltage vector of the two 3-phase sets  $\mathbf{v}_{dq,1}$  and  $\mathbf{v}_{dq,2}$  can be written in synchronous coordinates:

$$\begin{cases} \mathbf{v}_{dq,1} = R_s \mathbf{i}_{dq,1} + \frac{d\lambda_{dq,1}}{dt} + \mathbf{J}\omega \lambda_{dq,1} \\ \mathbf{v}_{dq,2} = R_s \mathbf{i}_{dq,2} + \frac{d\lambda_{dq,2}}{dt} + \mathbf{J}\omega \lambda_{dq,2} \end{cases} \quad (1)$$

where  $R_s$  is the stator resistance,  $\omega$  is the electrical angular frequency and  $\mathbf{J}$  is the complex operator matrix. The non-linear relationships between flux linkages and currents hold:

$$\begin{cases} \lambda_{dq,1} = \lambda_{dq,1}(\mathbf{i}_{dq,1}, \mathbf{i}_{dq,2}) \\ \lambda_{dq,2} = \lambda_{dq,2}(\mathbf{i}_{dq,1}, \mathbf{i}_{dq,2}) \end{cases} \quad (2)$$

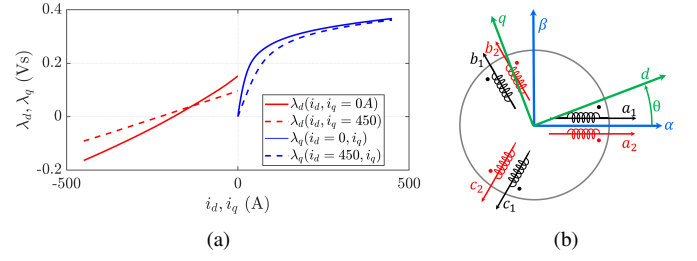


Fig. 2. (a) Saturation flux maps of the motor under test. (b) Definition of  $abc$ ,  $\alpha\beta$  and  $dq$  coordinates.

Fig. 1 determines the positive sign of the phase currents. The magnetizing current vector  $\mathbf{i}_{dq}$  is defined as:

$$\mathbf{i}_{dq} = \mathbf{i}_{dq,1} + \mathbf{i}_{dq,2} \quad (3)$$

The flux linkage in each 3-phase set is the sum of a magnetizing and a leakage term:

$$\begin{cases} \lambda_{dq,1} = \lambda_{dq} + L_\sigma \mathbf{i}_{dq,1} \\ \lambda_{dq,2} = \lambda_{dq} + L_\sigma \mathbf{i}_{dq,2} \end{cases} \quad (4)$$

where  $L_\sigma$  is the leakage inductance. The magnetizing flux is retrieved from the common mode flux and current:

$$\lambda_{dq} = \frac{\lambda_{dq,1} + \lambda_{dq,2}}{2} - L_\sigma \frac{\mathbf{i}_{dq,1} + \mathbf{i}_{dq,2}}{2} \quad (5)$$

The relationship between  $\mathbf{i}_{dq}$  and  $\lambda_{dq}$  is given by the flux maps in Fig. 2(a).

#### A. Zero Torque Locus

The motor torque can be computed as:

$$T = \frac{3}{2} p (\lambda_d i_q - \lambda_q i_d) \quad (6)$$

Being the machine under test an anisotropic PMSM, the torque is a combination of PM and reluctance torque. These two components have opposite sign for  $i_d > 0$ , and in particular a trajectory can be identified crossing the first and fourth quadrant of the  $dq$  plane where their effect is equal and opposite. If the magnetizing current vector  $\mathbf{i}_{dq}$  lies on such trajectory, called Zero Torque Locus (ZTL) [18], the developed shaft torque is null. For each point of the ZTL:

$$\lambda_d i_q = \lambda_q i_d \quad (7)$$

Fig. 3 shows the torque contour of the machine under test, with the ZTL highlighted in blue. This control law will be used for imposing zero torque during battery charge operation.

### IV. PROPOSED INTEGRATED OBC

#### A. General Concept of IFI-OBC

The general concept of the Isolated Fully-Integrated OBC (IFI-OBC) is to use the 6-phase PMSM as an isolation transformer and the inverter for controlling the energy conversion. This concept was proposed [13], both for 1-phase and 3-phase input grid, with two solutions named IFI-1ph and IFI-3ph OBC

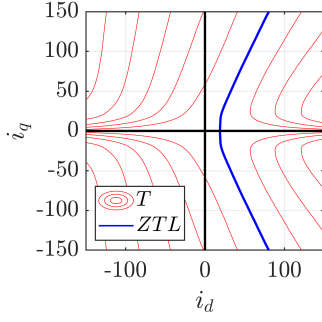


Fig. 3. Red: torque contour in the  $dq$  plane of the machine under test. Blue: zero torque locus.

respectively. This work further develops the single-phase IFI-OBC by introducing an innovative modulation strategy and a different control scheme, as later detailed. As visible from Fig. 4, the IFI-OBC does not employ additional electrical hardware respect to the drive itself. The grid terminals are directly connected to the motor phases without line filters.

Respect to the base configuration of the e-axis (see Fig. 1), INV.1 is disconnected, while the output of two phases ( $b_1$  and  $c_1$  in the Figure) of the same 3-phase set are connected to the grid outlet. The third phase is floating. The INV.2 is normally connected to the correspondent winding without any alteration.

The grid imposes a sinusoidal voltage excitation between the phases  $b_1$  and  $c_1$ , producing a pulsating flux in  $\alpha\beta$  coordinates. Since the two 3-phase sets are magnetically coupled, such pulsating excitation flux is linked to the phases  $b_2$  and  $c_2$ . The PMSM works as an insulating transformer, exploiting the magnetic coupling between the phases of the different sets.

#### B. Need for Number of Turns Reconfiguration

The main issue is that, since the primary winding of the equivalent transformer is directly connected to the grid, the amplitude of the magnetizing flux is determined by the grid voltage amplitude and frequency. Considering a phase voltage of 230 Vrms @ 50 Hz, the resulting peak flux amplitude is approximately 1 Vs, which is too high for the PMSM under test (see Fig. 2(a)). Therefore, the IFI-OBC is applicable assuming the motor windings can be reconfigured to increase the number of turns during charging. If the number of turns is increased by a factor  $n$ , the magnetizing flux and current  $\lambda'_{dq}$  and  $i'_{dq}$  in the reconfigured machine will be:

$$\lambda'_{dq} = n \cdot \lambda_{dq} \quad i'_{dq} = \frac{1}{n} \cdot i_{dq} \quad (8)$$

Such reconfiguration can be done, for example, by switching the pole pairs connection from parallel to series. Being  $p=3$  in the considered application, in this work we assume  $n = 3$ .

#### C. Avoiding Alternating Torque During Charge

As said, the OBC should not produce torque during charging. This is obtained by forcing the magnetizing current  $i_{dq}$  to be on the ZTL, i.e. the trajectory of the  $dq$  plane where PM and reluctance torque are even. To do so, it is necessary that

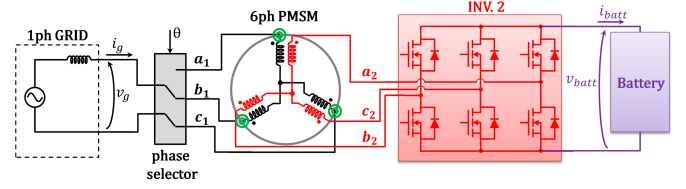


Fig. 4. Proposed IFI-1ph OBC topology.

the magnetic flux linkage produced by the grid excitation is as close as possible to the  $q$  axis. Two methods are proposed here to obtain this result.

The first solution is to align the rotor along a proper direction using a DC current vector (rotor parking). As an example, if the grid is connected between the phases  $b_1$  and  $c_1$ , as in Fig. 4, the grid excites the machine in  $\beta$  direction, so the rotor should be aligned with the  $d$  axis along  $\alpha$  direction ( $\theta = 0$ ). In this way, the machine will receive by the grid a pulsating excitation in  $q$  axis, and the control will be able to move the  $i_{dq}$  vector on the ZTL. Being the phase  $a_1$  not connected, the vector  $i_{dq,1}$  will necessarily lay on  $\beta$  axis.

This first method requires the possibility to align the motor along a specific direction, which may be feasible or not depending on the e-axis topology. It must be considered that most of the modern EV present a transmission gearbox connecting the motor to the wheel shaft, with typical reduction ratio of  $8 \div 12$ . As an example, if the gearbox is equipped with a disconnect clutch, this can be used for mechanically separating the rotor and so permitting its freeshaft parking. If the clutch is not present, aligning the  $d$  axis along  $\beta$  direction would require a rotation of maximum  $\pm 90^\circ$  in electrical coordinates (worst case situation), corresponding to  $\pm 30$  mechanical degrees at the rotor shaft. Considering the transmission gearbox, this would produce a linear movement of the car lower than 2 cm. With no clutch, this solution is normally not acceptable.

The second option proposed here is valid in general, with or without disconnecting clutch, and consists of properly select the phases of the first 3-phase set to be connected to the grid depending on the rotor position, so that the flux produced by the grid excitation is as close as possible to the  $q$  axis. The  $\theta$ -dependent phase selector of Fig. 4 is included in the scheme to this purpose. In this way, the deviation between the magnetizing current and the  $q$  axis is minimized. The rotor will not move from its initial position, which is random, without necessarily being locked since no torque is produced.

In particular, the grid will be connected between the phases  $b_1$  and  $c_1$  as in Fig. 4 if the rotor position is between  $\pm 30^\circ$  or between  $150^\circ$  and  $210^\circ$ . If the initial position is between  $30^\circ$  and  $90^\circ$  or between  $210^\circ$  and  $270^\circ$  the grid will be connected between the terminals  $a_1$  and  $b_1$ , thus the excitation flux imposed by the grid will have a phase of  $-30^\circ$ . Otherwise, the phases  $a_1$  and  $c_1$  will be adopted (excitation flux at  $30^\circ$ ). The phase selection scheme depending on the rotor position is reported in Fig. 6. The flux excitation imposed by the grid

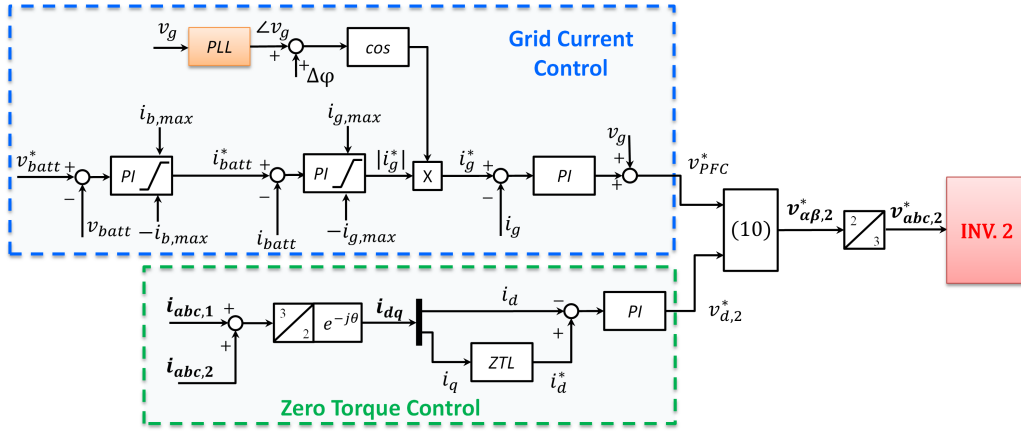


Fig. 5. Block diagram for grid current control for IFI-1ph configuration.

will not fall exactly on  $q$  axis, but it will have a deviation of maximum  $\pm 30^\circ$  in the worst case.

In the following, an initial rotor position between  $\pm 30^\circ$  will be considered, so the grid is connected between the phases  $b_1$  and  $c_1$ . The other cases having different rotor position can be easily retrieved by permuting the names of the phases, so they will not be reported here for sake of brevity.

#### D. Charge control with Power Factor Correction

The control of the grid current is obtained by a cascaded control, shown in Fig. 5 (blue box). An external voltage loop sets the reference battery current amplitude  $i_{batt}^*$  in order to obtain the desired voltage at the battery terminals. The reference  $v_{batt}^*$  is compared with the measured value  $v_{batt}$  and the discrepancy is input to a PI regulator, whose output is saturated at the maximum charging current. This permits to control the charging process either in CC (for low battery SOC) or CV (for high SOC) mode. Then, the error between  $i_{batt}^*$  and the measured  $i_{batt}$  is input to a second PI regulator, obtaining the reference amplitude of the grid current  $i_g^*$ .

The inner loop is a non-conventional current control loop. The grid current  $i_g$  is controlled by the PI regulator to the right end of the dashed box. This is the current in the primary side

of the equivalent transformer, flowing through two phases of the first 3-phase set (phases  $b_1$  and  $c_1$  in the example of Fig. 4. The output of the PI regulator (enhanced by a feed-forward of  $v_g$ ), called  $v_{PFC}^*$ , sets the projection of  $v_{\alpha\beta,2}^*$  along the direction of the grid excitation in the battery side ( $\beta$  axis in the example).

Since the inverter switching frequency (12 to 50 kHz) is much higher than the grid frequency (50 Hz), a PI regulator is normally sufficient for accurate control of  $i_g$ . If needed, a resonant controller can be adopted instead.

The phase of the grid voltage is extracted by a Phase Locked Loop (PLL) structure. The PLL type and dynamics are not deeply affecting the performance of the proposed OBC, so it will not be further discussed here. Several PLL present in the literature are suitable for a reliable grid phase estimation [19].

If required by the TSO, a phase shift  $\Delta\varphi$  between grid voltage and reference current can be introduced for generating or absorbing reactive power from the grid. If a unitary PF is required, the reference phase shift  $\Delta\varphi$  is set to zero.

#### E. Zero Torque Control

For avoiding torque production during charge, the magnetizing current vector  $i_{dq}$  is forced to lay on the ZTL with a second non-conventional current control loop, according to the block diagram of Fig. 5. For doing so, the ZTL trajectory in the  $dq$  plane must be offline retrieved based on the machine flux maps, depicted in Fig. 2(a). In particular, the following function is needed:

$$i_{d,ZTL} = i_{d,ZTL}(i_q) \quad (9)$$

where  $i_{d,ZTL}$  is the value of  $i_d$  that meets the ZTL for a given  $i_q$ . This function is graphically depicted in Fig. 7.

The magnetizing current  $i_{dq}$  is computed from the measured phase currents in the two 3-phase sets (3). Because of the initial parking, or because of the initial phase selection, the current in  $q$  axis is mostly determined by the grid voltage excitation and grid current control loop. The resulting  $i_q$  is adopted in (9) for retrieving the reference value of  $i_d^*$  which would drive the vector  $i_{dq}$  on the ZTL.

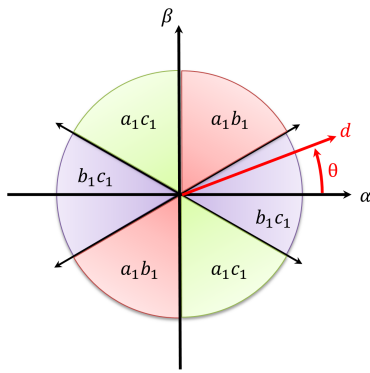


Fig. 6. Scheme for selecting the phases to be connected to the grid on varying the initial rotor position for the IFI-1ph OBC with active zero torque control.



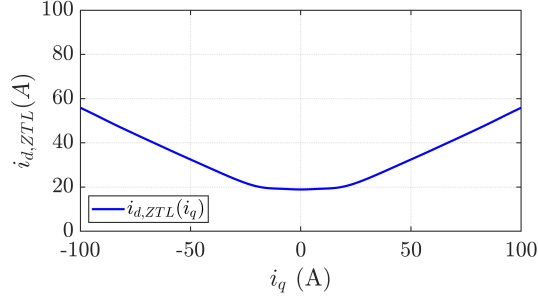


Fig. 7. Selection of  $i_d^*$  based on the measured  $i_q$ .

The reference  $i_d^*$  is then compared with the actual  $i_d$ , and the discrepancy is input to a PI regulator, whose output is the voltage in  $d$ -axis on the secondary side of the equivalent transformer, i.e.  $v_{d,2}^*$ .

#### F. Fusion of Current Control and Zero Torque Control

Finally, the computed  $v_{PFC}^*$  and  $v_{d,2}^*$ , adopted for controlling the grid current waveform and the shaft torque respectively, are combined for obtaining the reference 3-phase voltages of INV.2  $v_{abc,2}^*$  using a non-standard voltage control.

For doing so,  $v_{PFC}^*$  and  $v_{d,2}^*$  are combined to form the voltage vector  $v_{\alpha\beta,2}^*$ . Among these two components,  $v_{d,2}^*$  is always in the rotor direction having minimum inductance, with a phase shift  $\theta$  respect to  $\alpha$  axis (see Fig. 2(b)), while  $v_{PFC}^*$  is imposed in the direction of grid excitation, which depends on the phase selector, according to Fig. 6.

In the specific case where the grid is connected between  $b_1$  and  $c_1$ , as in the reported example, the grid excitation direction coincides with  $\beta$  axis, so  $v_{PFC}^* = v_{\beta,2}^*$ . In this case,  $v_{PFC}^*$  and  $v_{d,2}^*$  are combined through the following expression:

$$\begin{bmatrix} v_{\alpha,2}^* \\ v_{\beta,2}^* \end{bmatrix} = \begin{bmatrix} \frac{1}{\cos(\theta)} & \tan(\theta) \\ 0 & 1 \end{bmatrix} \begin{bmatrix} v_{d,2}^* \\ v_{PFC}^* \end{bmatrix} \quad (10)$$

This expression can be generalized to include the other cases of phase selection (grid connected between  $a_1$  and  $b_1$  or between  $a_1$  and  $c_1$ ), correspondent to different rotor positions. The generalized expression is not reported here for brevity.

Finally, the canonical Clarke transformation is employed for computing the 3-phase reference voltages for INV.2  $v_{abc,2}^*$ .

It must be noted that the components  $v_{PFC,2}$  and  $v_{d,2}$  used in (10) for defining  $v_{\alpha\beta,2}^*$  are not orthogonal. This would lead to instability if the  $d$  and grid excitation axes were close each others. Anyway, as previously described, thanks to the phase selection in Fig. 6 or to the rotor parking the two axes have a minimum displacement of  $60^\circ$ , thus avoiding instability.

### V. SIMULATION RESULTS

The proposed IFI OBC was validated by extensive simulations using PLECS software. As in (8), to avoid excessive core saturation the number of turns is virtually increased by 3 times ( $n=3$ ), assuming the winding configuration of the poles connections is switched from all pairs in parallel to all in series.

The topology of Fig. 4 was tested for two different rotor positions, controlled with the structure in Fig. 5 while the maximum power was absorbed from the grid (6.3 kW). As said, the considered rotor phase angle is bounded between  $-30^\circ < \theta < 30^\circ$ , compatible with having the grid connected between the pahses  $b_1$  and  $c_1$  as in this example. So, the grid voltage corresponds to  $v_{bc,1}$ , the grid current is equal to  $i_g = i_b = -i_c$  and the induced voltage on the battery side is  $v_{bc,2}$  (see Section IV-A). The phase  $a_1$  is floating, so  $i_{a1} = 0$ .

In particular, in case a rotor parking is possible the rotor position will be  $\theta=0^\circ$ . The results referred to this case are depicted in Fig. 8. The upper subplot shows the grid side voltage and current. As can be seen, the current is properly controlled to be in phase with the grid voltage, with  $\text{PF} \approx 1$  and a  $\text{THD} < 1.5\%$ . Therefore, the standard requirements [16] are well respected. The lower plot of the same Figure reports the correspondent voltage and current on the battery side of the PMSM, showing a similar voltage but a lower PF. This can be explained considering that the PMSM is acting as a transformer, so it has to absorb reactive power for magnetizing the rotor. Since  $\text{PF}=1$  on the primary side, such reactive power is given by the secondary side of the machine.

The two subplots of Fig. 9 refer to the same test, with the rotor position  $\theta=30^\circ$ , i.e. the worst possible case of initial rotor position assuming the rotor parking is not applicable ( $q$  axis  $30^\circ$  away from  $\beta$  axis). In terms of mains current  $i_g$ , the

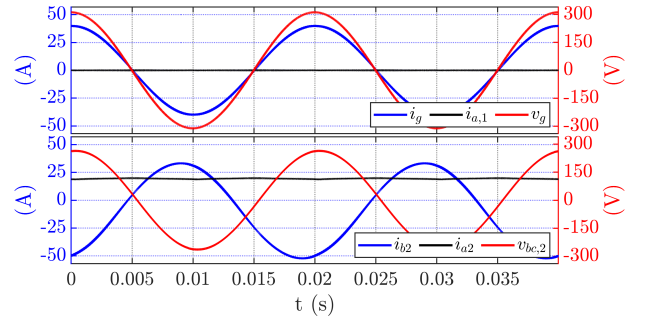


Fig. 8. IFI-1ph using initial parking ( $\theta=0^\circ$ ). Upper plot: current and voltage on grid side of the PMSM. Lower plot: Current and voltage on the battery side.

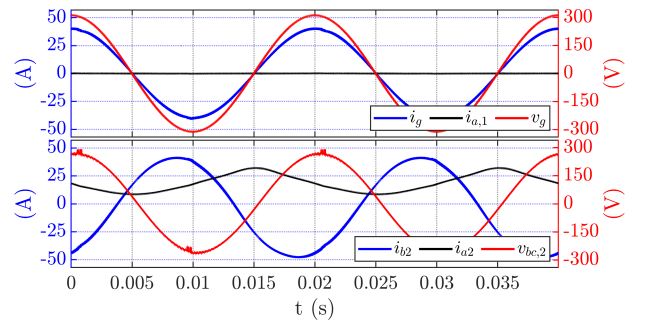


Fig. 9. IFI-1ph using active zero torque control with the worst case of initial position ( $\theta=30^\circ$ ). Upper plot: current and voltage on grid side of the PMSM. Lower plot: Current and voltage on the battery side.

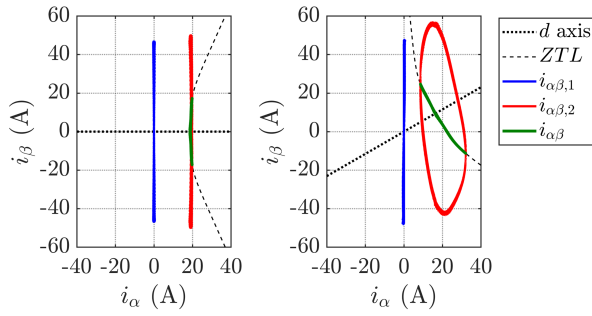


Fig. 10. Trajectories of primary, secondary and magnetizing currents in the  $\alpha\beta$  frame with (left) initial parking,  $\theta = 0$  and (right) worst case of initial position,  $\theta = 30^\circ$ .

difference respect to Fig. 8 is negligible (again  $\text{THD} < 1.5\%$ ,  $\text{PF} \approx 1$ ), since the adopted grid current control is the same. In other words, the IFI-1ph OBC is able to properly control the grid current regardless the initial rotor position.

The subplots in Fig. 10 show the trajectories depicted by the current vectors  $i_{\alpha\beta,1}$ ,  $i_{\alpha\beta,2}$  and the magnetizing current  $i_{\alpha\beta}$  in the  $\alpha\beta$  plane, again considering an initial parking ( $\theta=0^\circ$ ) and the worst case of initial position ( $\theta=30^\circ$ ). Being the  $a_1$  phase disconnected, in both cases the vector  $i_{\alpha\beta,1}$  moves along  $\beta$  axis. As can be seen, the second 3-phase set is mostly excited in the same direction, but the zero torque control loop moves the magnetizing current on the ZTL.

In the second subplot, the rotor is  $30^\circ$  shifted from  $\beta$  axis. The main excitation is still in  $\beta$  direction, while the zero torque control loop deviates the magnetizing current vectors, still on the ZTL. Again, the zero torque control loop is properly working whatever the rotor position.

Finally, Fig. 11 shows the torque in the two tested rotor position. In both cases the proposed techniques work very well, as negligible torque is obtained. It should be remarked that without actively controlling  $T = 0$ , the torque at the shaft would be very high.

Overall, the simulation results are promising, demonstrating effective charging capability with negligible torque production.

## CONCLUSIONS

This work deals with a new zero torque control scheme for an integrated battery charger for EVs with 6-phase PMSM. The motor is exploited as transformer to obtain galvanic isolation between the power grid and the EV battery, not provided by existing integrated solutions. Appropriate control techniques was developed, made of two non-standard current control loops: the first is adopted to control the grid current waveform and charging power, the second for guaranteeing that no torque is produced during charging stage. Extensive simulation results confirm the proposed solution is promising, with good charging control capability.

## ACKNOWLEDGMENTS

The authors are grateful to the European Commission for the support to the present work, performed within the EU H2020 project FITGEN (Grant Agreement 824335).

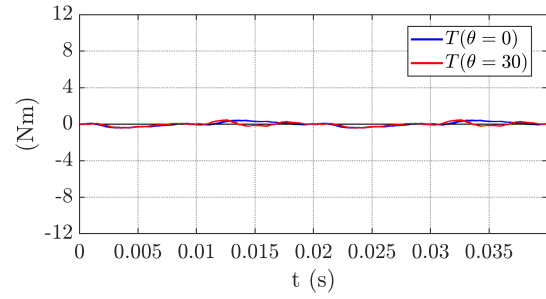


Fig. 11. Shaft torque using initial alignment (blue line) and active zero torque control with the worst case initial position, i.e.  $\theta=30^\circ$  (red line).

## REFERENCES

- [1] European Roadmap Electrification of Road Transport, 3rd Edition, Version: 10, June 2017.
- [2] E. Levi, "Multiphase Electric Machines for Variable-Speed Applications," in *IEEE Transactions on Industrial Electronics*, vol. 55, no. 5, pp. 1893-1909, May 2008.
- [3] M. De Gennaro et Al., "Interim results of the H2020 project FITGEN: design and integration of an e-axle for the third-generation electric vehicles," *2020 World Electric Vehicle Symposium and Exposition (EVS33)*, Portland, OR, 2020.
- [4] A. Khaligh and S. Dusmez, "Comprehensive Topological Analysis of Conductive and Inductive Charging Solutions for Plug-In Electric Vehicles," in *IEEE Trans. on Vehicular Technology*, Oct. 2012.
- [5] L. Solero, "Nonconventional on-board charger for electric vehicle propulsion batteries," in *IEEE Transactions on Vehicular Technology*, vol. 50, no. 1, pp. 144-149, Jan. 2001.
- [6] L. De Sousa, B. Silvestre and B. Bouchez, "A combined multiphase electric drive and fast battery charger for Electric Vehicles," *2010 IEEE Vehicle Power and Propulsion Conference*, Lille, 2010, pp. 1-6.
- [7] G. Pellegrino, E. Armando and P. Guglielmi, "An Integral Battery Charger With Power Factor Correction for Electric Scooter," in *IEEE Transactions on Power Electronics*, vol. 25, no. 3, pp. 751-759, 2010.
- [8] S. Lacroix, E. Laboure and M. Hilaret, "An integrated fast battery charger for Electric Vehicle," *2010 IEEE Vehicle Power and Propulsion Conference*, Lille, 2010, pp. 1-6.
- [9] US Patent US8847555B2, "Fast charging device for an electric vehicle".
- [10] I. Subotic and E. Levi, "An integrated battery charger for EVs based on a symmetrical six-phase machine," *2014 IEEE 23rd International Symposium on Industrial Electronics (ISIE)*, Istanbul, 2014.
- [11] I. Subotic and E. Levi, "A review of single-phase on-board integrated battery charging topologies for electric vehicles," *2015 IEEE Workshop on Electrical Machines Design, Control and Diagnosis (WEMDCD)*, Torino, 2015, pp. 136-145.
- [12] S. Hagbabin, S. Lundmark, M. Alakula and O. Carlson, "Grid-Connected Integrated Battery Chargers in Vehicle Applications: Review and New Solution," in *IEEE Transactions on Industrial Electronics*, 2013.
- [13] P. Pescetto and G. Pellegrino, "Integrated Isolated OBC for EVs with 6-phase Traction Motor Drives," *2020 IEEE Energy Conversion Congress and Exposition (ECCE)*, Detroit, MI, USA, 2020.
- [14] F. Barrero and M. J. Duran, "Recent Advances in the Design, Modeling, and Control of Multiphase Machines—Part I," in *IEEE Transactions on Industrial Electronics*, Jan. 2016.
- [15] P. Xu, J. H. Feng, S. Y. Guo, S. Feng, W. Chu, Y. Ren, Z. Q. Zhu, "Analysis of Dual Three-Phase Permanent-Magnet Synchronous Machines With Different Angle Displacements," in *IEEE Trans. on Industrial Electronics*, vol. 65, no. 3, pp. 1941-1954, 2018.
- [16] International standard IEC 61851-1:2017-02
- [17] P. B. Andersen, et al., "Innovation outlook: Smart charging for electric vehicles," Int. Renewable Energy Agency, 2019. [Online]. Available: [https://www.irena.org/-/media/Files/IRENA/Agency/Publication/2019/May/IRENA\\_Innovation\\_Outlook\\_EV\\_smart\\_charging\\_2019.pdf](https://www.irena.org/-/media/Files/IRENA/Agency/Publication/2019/May/IRENA_Innovation_Outlook_EV_smart_charging_2019.pdf)
- [18] P. Pescetto and G. Pellegrino, "Determination of PM Flux Linkage Based on Minimum Saliency Tracking for PM-SyR Machines Without Rotor Movement," in *IEEE Transactions on Industry Applications*.
- [19] R. Best, "Phase Locked Loops: Design, Simulation, and Applications", 6th edition, McGraw-hill, 2007